Primary-Side Power Flow Control of Wireless Power Transfer for Electric Vehicle Charging

John M. Miller, *Fellow, IEEE*, Omer C. Onar, and Madhu Chinthavali

***Abstract*— Various noncontacting methods of plug-in electric vehicle charging are either under development or now deployed as aftermarket options in the light-duty automotive market. Wireless power transfer (WPT) is now the accepted term for wireless charging and is used synonymously for inductive power transfer and magnetic resonance coupling. WPT technology is in its infancy; standardization is lacking, especially on interoperability, center frequency selection, magnetic fringe field suppression, and the methods employed for power flow regulation. This paper proposes a new analysis concept for power flow in WPT in which the primary provides frequency selection and the tuned secondary, with its resemblance to a power transmission network having a reactive power voltage control, is analyzed as a transmission network. Analysis is supported with experimental data taken from Oak Ridge National Laboratory's WPT apparatus. This paper also provides an experimental evidence for frequency selection, fringe field assessment, and the need for low-latency communications in the feedback path.**

***Index Terms*— EV charging, inductive power transfer, wireless power transfer.**

NOMENCLATURE

AFE	Active front end.
CPT	Contactless power transfer.
CWT	Coaxial winding transformer.
DWPT	Dynamic wireless power transfer.
EREV	Extended-range electric vehicle.
ESS	Energy-storage system.
IGBT	Insulated gate bipolar transistor.
INV	Inverter, dc-to-ac conversion.
IPT	Inductive power transfer.
LCL	Inductor–capacitor–inductor.
LiC	Lithium capacitor.
ORNL	Oak Ridge National Laboratory.
OBC	On board charger.
PEV	Plug-in electric vehicle.
PFC	Power factor corrector.
SBD	Schottky barrier diode.
SOC	State of charge.
V2I	Vehicle to infrastructure.
VAR	Volt-Ampere-Reactive.
WPT	Wireless power transfer.
WPTB	Wireless charger base unit.

Manuscript received December 11, 2013; revised March 10, 2014; accepted March 12, 2014. Date of publication December 22, 2014; date of current version January 29, 2015. This manuscript has been authored by Oak Ridge National Laboratory, operated by UT-Battelle, LLC under Contract No. DE-AC05-00OR22725 for the U.S. Department of Energy. The United States Government retains and the publisher, by accepting the article for publication, acknowledges that the United States Government retains a non-exclusive, paid-up, irrevocable, world-wide license to publish or reproduce the published form of this manuscript, or allow others to do so, for United States Government purposes. The Department of Energy will provide public access to these results of federally sponsored research in accordance with the DOE Public Access Plan (energy.gov/downloads/doe-public-access-plan). Recommended for publication by Associate Editor Chris Mi and Chun Rim.

The authors are with the Oak Ridge National Laboratory, Power Electronics and Electric Machinery Group, National Transportation Research Center, Energy and Transportation Science Division, Oak Ridge, TN 37932 USA (e-mail: jmmiller35@aol.com; onaroc@ornl.gov; chinthavalim@ornl.gov).

Color versions of one or more of the figures in this paper are available online at http://ieeexplore.ieee.org.

Digital Object Identifier 10.1109/JESTPE.2014.2382569

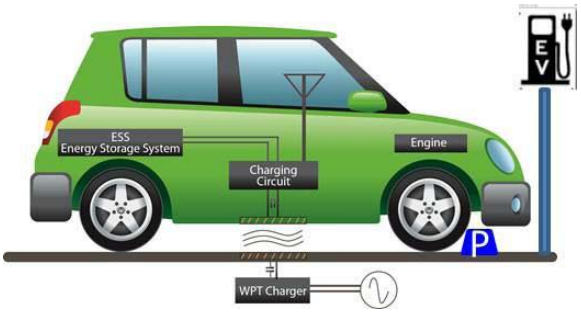

Fig. 1. Concept of WPT charging of PEV.

I. INTRODUCTION

THE field of wireless charging of PEVs has grown tremendously in recent years to the point that today several companies offer commercial wireless chargers as aftermarket products for integration into light-duty passenger vehicles [1]. WPT can be viewed as a revolutionary step in PEV charging, because it fits the paradigm of V2I, wirelessly. Benefits of WPT are well known as a safe, convenient, flexible, and autonomous means of passenger vehicle charging that has the potential to completely displace today's conductive charging; WPT is a disruptive technology. There are no cables to trip over, no heavy plugs and cabling to wrestle with during inclement weather, and no concerns about inadvertent disconnection. Wireless charging of EVs represents a significant step in the context of connected vehicle, wireless communications, and eventually, with the in-motion charging of EVs, the ultimate in autonomous vehicle operation; dynamic wireless charging.

Fig. 1 shows stationary wireless charging that is enabled by the existing standards and hardware for private and secure wireless communications. It is stationary charging technology in that power transfer takes place in a residential garage, car port, or public parking structure when the WPT-equipped vehicle is simply parked over a charging pad on or embedded into the floor. Recharging the PEV ESS is autonomous, and follows a state control algorithm built into the base WPT controller. The communication sequence consists of V2I short-range messaging to acknowledge the charger location, operational

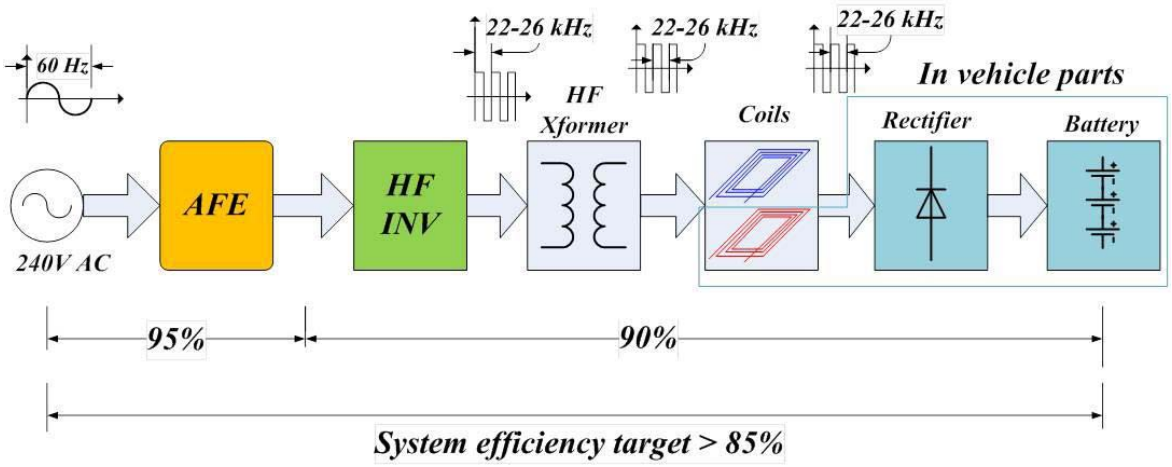

Fig. 2. WPT functional cascade and overall efficiency goals.

status, and to aid in alignment. Once the appropriate handshaking is complete between the PEV and the WPT base unit (WPTB) its HF inverter provides excitation current to the tuned primary coil at a standardized center frequency. Power is transferred across a nominal gap that is on the order of the PEV ground clearance. HF secondary power is rectified, filtered, and delivered to the ESS. Incremental frequency adjustment needed to accommodate gap variations in the coupler is done automatically in the WPTB controller power-tracking algorithm. Power flow sensing, communications, and grid-side regulation complete the regulation loop via the radio channel.

Fig. 2 shows the functional blocks involved in the power transmission path. Utility ac power is converted to controllable dc voltage by the AFE comprising a PFC stage. Adjustable dc voltage is applied to the high-power rails of a HF full-bridge inverter having selectable duty ratio. The HF stage delivers excitation current to a series-tuned primary coil of sufficient magnitude to magnetize the air volume between it and the vehicle-mounted secondary, or capture coil. Voltage induced at the secondary is rectified, filtered, and delivered to the vehicle HV battery either directly from the WPT rectifier or indirectly via the vehicle OBC. WPT applications may require inclusion of an HF transformer to provide electrical isolation of the WPT primary pad and cabling from the utility. However, treatment of isolation requirements, grid power quality, and PEV HF ripple current are the subjects of ongoing deliberation in standardization activities by the Society of Automotive Engineers (SAE) [2]. The SAE J2954 chair [2] coordinates activities related to interoperability, health and safety, communications, and field measurement of WPT. For the purposes of this paper, it can be appreciated that meeting high-efficiency goals entails no more than 3% loss in each of the five stages of cascade shown in Fig. 2: 1) PFC; 2) HF inverter; 3) HF transformer; 4) coupling coils; and 5) rectifier/filter. This means that for matched and interoperable WPT installations that are used for PEV charging, the overall efficiency must be $>85\%$. How this can be achieved is also a purpose of this paper.

There is now a rapidly growing volume of research literature on WPT (also IPT or CPT) that in this paper is viewed as falling into one of five categories: 1) WPT research to maximize efficiency; 2) power flow control and optimization; 3) the physics of WPT, including the use of soft ferrites, Litz cable, and electromagnetic theory; 4) cross-cutting applications, such as WPT in medical, marine, aerospace, and other applications; and 5) future dynamic or in-motion wireless charging.

A. Maximizing WPT Efficiency

In the recent literature, the focus has been on coupling coil design, electrical quality of the secondary side, and the use of power electronic-based reactive power control. Strong emphasis is placed on primary and secondary sides in [3]. The key feature of this paper is the emphasis on tuning procedure, semiresonant Class-E operation of the HF inverter, and resistive load. Ning *et al.* [4] and Miller *et al.* [5] provide full details of coupling coil design, the fabrication sequence, characterization data, and experimental results for WPT performance, including misalignment tolerance and its influence on efficiency. Additional details on frequency tracking to improve efficiency are found in [6] and a summary of issues and challenges is provided in [7] complimenting this topic.

B. Power Flow Control and Optimization

Miller and Onar [8] provide in-depth analysis and experimental results for WPT power flow control and experimental results. In this paper, the WPT system is primary-side-controlled, relies on minimal secondary-side electronics for compactness and cost, and utilizes private and secure wireless communications in the power regulation feedback path. Huang *et al.* [9] expand on their considerable earlier WPT work, and in [10], they present a new control strategy for series–parallel (S–P)-tuned, unity power factor, LCL pickup that utilizes minimal power electronics. The use of power electronics for reactive power control does have a penalty in utility connection to secondary dc output efficiency as noted in [9], showing efficiency of 80% at full power and 70% at half power. Chinthavali *et al.* [11], Ning *et al.* [12], and Miller *et al.* [13] investigate the power electronic regulation of secondary-side power via active rectification and the employment of genetic algorithms, and focus on grid-side

power flow control. In a similar fashion, Chao *et al.* [14], [15] and Li *et al.* [16] also focus on primary-side control and optimization and provide solid theoretical basis for primary-side regulation. The use of power electronics for WPT voltage control is developed extensively for the asymmetric case [17] and for symmetric voltage cancellation [18]. Power flow control is tied in with coupling coil design in [19] and [20]. Additional scope and insights for noncontacting power flow control are found in [21]–[24].

C. Physics of WPT and Electromagnetics

The entire field of WPT charging of PEVs owes its existence to early investigations into the physics of coupled circuits [25] and inductance calculations of separated coils [26], including calculations on the flux from circular loops. Other researchers have investigated WPT in the context of HF helical antenna [27], [28], all of which has its foundation in coupled circuit theory [29] and antenna theory relevant to WPT [30]. The need for field shaping and shielding afforded by the use of soft magnetic materials, such as low-loss ferrites, for WPT was investigated in [31] and [32]. Sibué *et al.* [31] describe the use of Ferroxcube 3C90 low-loss ferrite E-cores in a 1.6 kW, 300 V_{dc}, and 100-kHz WPT. Of major concern for WPT is the effect of skin depth in conductors energized with HF current and the attendant proximity effects when conductors are formed into coils. Mizuno *et al.* [33] and Shinagawa *et al.* [34] focus on the use of magnetoplated wire as a means to reduce proximity effects in spiral wound coils for use as induction heating appliances. The use of ferrites in WPT back-plane structures, the need for Litz cable, and pressing need for standardization are discussed in [35]–[37].

D. Cross-Cutting Applications

It is not just the experience and component knowledge gained from the field of induction heating that applies to WPT, but from work in other fields in which power must be delivered across working gaps that include biologic or insulating materials. Si *et al.* [38] are a case in point. In this paper, the efficiency of the secondary pickup in WPT is of paramount importance, because energy dissipation will heat the surrounding tissue even when the overall efficiency is on the order of 90%. In medical applications based on the implantable devices, it is mandatory that primary-side voltage regulation is used; consequently, primary-side frequency adjustment is necessary to tune or detune the secondary according to variable load requirements. Specific cases of implanted medical devices, such as left ventricular assist device (LVAD), drug infusion devices, and artificial heart, are cited as opportunities for WPT. The LVAD may require up to 30 W of delivered power through a WPT coil pair operating in the 50–500-kHz range, with coupling coefficient in the range of 0.1–0.3, using parallel-tuned secondary coil, and working gaps up to 30 mm. In another example, Kelly and Owens [39] describe noncontacting power delivery to in-seat entertainment systems in passenger aircraft, where conductive power delivery is problematic due to connector reliability and the provision for seat rearrangement. In this CPT system, an E-core primary consisting of two windings in parallel is used to couple power to a moveable secondary pickup consisting of a C-core aligned to two slots of the primary E-core. Power transfer of 52 W (5 V $\sim$ 10 A) at 28 kHz was the stated design criteria. Another example of early work was the application of WPT for powering robots, machine tools, and moveable systems, as presented in [40], in which a pair of 400-mm diameter coils was designed to deliver 1 kW across a 300-mm gap when operated at 100 kHz, S–P tuned, demonstrating an overall efficiency of 80%.

E. Dynamic Wireless Charging

Easily the most intriguing of all WPT applications is the in-motion charging, which shows promise for advanced electrified highway systems of the future. Smeets *et al.* [41] describe a contactless energy transfer (CET) apparatus for delivering power to a moving load, such as MAGLEV transportation, rope-less elevators, and on-road charging of PEVs. In the CET, the primary consists of multiple switched coils and a single, large pitch, secondary coil that spans two primary coils. The innovation in CET for long stroke linear motors is that actively controlling individual primary coils overcome the large primary leakage inductance of long-run primary-cable-type systems. Jung *et al.* [42] provide the most recent technical updates for in-motion WPT in their online electric vehicle technology, having a major innovation in the supply of dc along the energized track together with the use of distributed HF power inverters. Onar *et al.* [43] and Miller and Onar [44] describe a multiple, switched coil, primary energized track for in-motion charging of a PEV along with experimental results obtained from a Global Electric Motorcar (GEM) demonstration vehicle. Early results for the online EV system described in [42] are provided in [45]–[47]. Similarly, early works pertaining to the results for in-motion WPT charging [43], [44] are provided in [48]–[52]. The salient issues of dynamic WPT are speed dependence, pulsating power delivery to the PEV's ESS, and its attendant pulsating burden reflected to the utility point of common connection, neither of which have good consequences. PEV batteries do not tolerate either high ripple current or pulsating charging power and in fact will deteriorate and age faster. At the utility, and for energized tracks in both directions of traffic flow, the highly intermittent pulse loading is problematic for grid demand response and stability. Miller *et al.* [53] discuss in detail the use of high-power electrochemical capacitors to smoothen power pulsations at grid side using LiCs in active parallel with the grid-connected power supply, and with symmetric carbon ultracapacitors in passive parallel with the GEM vehicle battery pack, plus the same architecture but with lithium caps in the vehicle, and concluding with both grid-side and in-vehicle power capacitor smoothing.

II. ORNL Wireless Charging System

ORNL has investigated WPT since 2008, with considerable progress made in the analysis, design, material selection, and performance assessment of stationary and in-motion WPT.

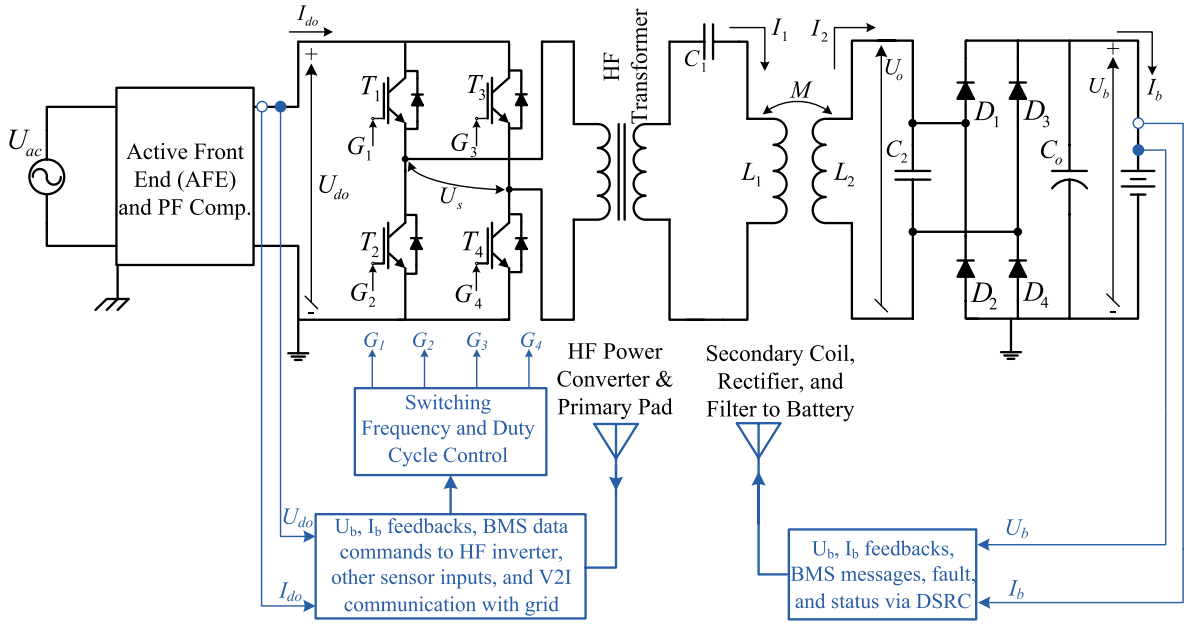

Fig. 3. Architecture of primary-side regulation of WPT charging.

TABLE I
WIRELESS CHARGING SYSTEM PARAMETERS FOR SYSTEM IN FIG. 3

Stage	Symbol	Value	Unit	Stage	Symbol	Value	Unit
Utility	U_{ac}	220	(V_{rms})	HF Transformer	Ratio, a	3.75:1	(#)
	I_{max}	60	(A_{rms})		Core	3C90	(Mat'l)
Load	P_0	10	(kW)		Pri (Litz)	6	(AWG)
	Eff	>0.85	(#)		Sec (Litz)	2	(AWG)
PFC	PF	>95	(%)	Coupling coil	a_{1eq}	256	(mm)
	THD	<5	(%)		a_{2eq}	249	(mm)
	U_{do_min}	340	(V_{dc})		N_{pri}	11	(#)
	U_{do_max}	800	(V_{dc})		Lpri	122	(μH)
Rectifier	U_{bat}	370	(V_{dc})		k(z=125)	>0.3	(#)
	I_{chg}	32	(A_{dc})		Lsec	122	(μH)
	δI_{chg}	<15	(A_{pp})		R_{ac}(25 kHz)	38	(mΩ)
gap	z	>100	(mm)		R_{ac}(48 kHz)	64	(mΩ)

Fig. 3 shows a high-level schematic representation of ORNL's primary-side-regulated WPT system that includes the five power conversion stages as discussed earlier. The essential elements of the ORNL's approach are several: 1) an AFE to maintain grid power quality using a boost; 2) an interleaved power factor corrector stage implemented with wide bandgap semiconductor devices; 3) a high-voltage power inverter using 1200 V silicon IGBT modules for operation at dc-link voltages from 340 to 800 V_{dc}; 4) a high-frequency CWT fabricated with low-loss ferrite (MnZn) for which higher flux density FeCo nanocomposite is being investigated for future use; 5) coupling coils (coupler) fabricated with Litz cable in a planar spiral winding over soft ferrite flux guides; and 6) a load rectifier using fast recovery diodes over the course of the past three years ORNL researchers have evaluated various tuning means and selected the *S–P* method as most appropriate for voltage source operation. The high-frequency rectifier on the secondary side was initially implemented using fast recovery silicon rectifiers of p-i-n structure, then replaced with lower switching loss SiC SBDs that yielded rectifier efficiencies averaging near 99% regardless of operating frequency in the 10–148-kHz WPT spectrum.

Specifications for the ORNL wireless charging equipment discussed in this paper are given for single-phase 220 V_{ac} input and a load power of 10 kW, as listed in Table I. The requirement for 10-kW WPT capability comes from the contract that ORNL and partners have with the U.S. Department of Energy (DOE) to develop stationary WPT suitable to

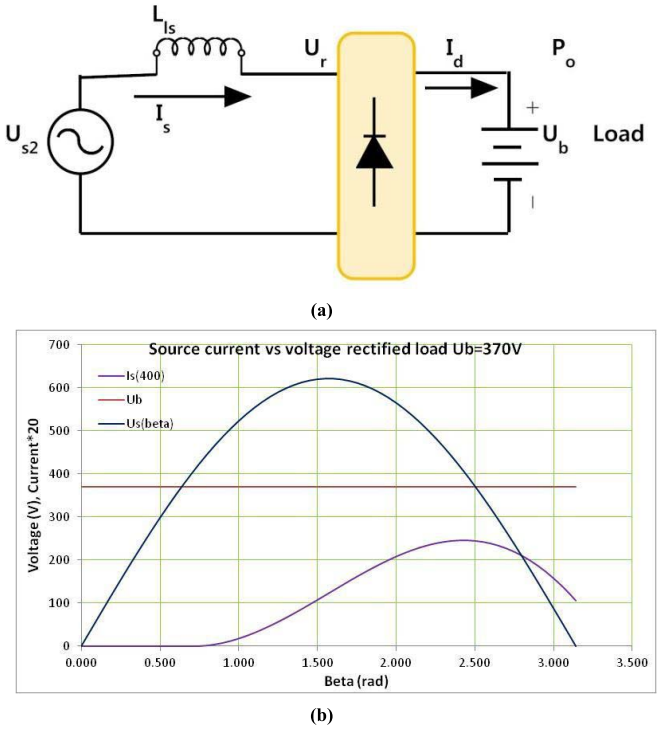

Fig. 4. (a) AC source-connected via line inductance to rectify constant voltage load. (b) Waveforms for $U_s = 400\ V_{\rm rms}, U_b = 370\ V_{\rm dc}$, and $I_s(\beta)$, $L_s = 122\ \mu$H for which $L_{ls} = (1 - k_z)\ L_{\rm pri} = 92.7\ \mu$H.

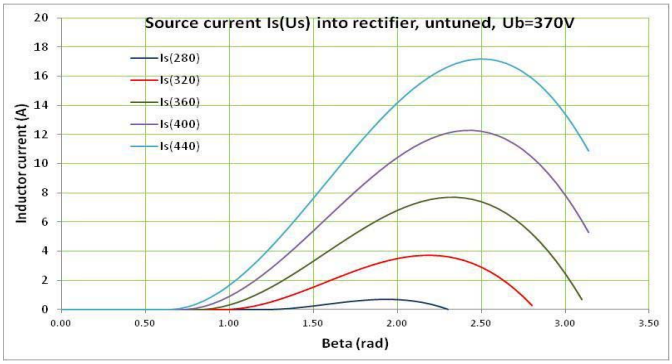

Fig. 5. Family of source current profiles with parameter $U_{s2} = 280$, 320, 360, 400, and 440 $V_{\rm rms}$.

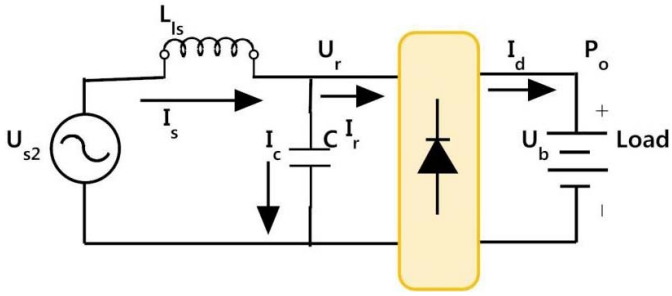

Fig. 6. Compensated secondary WPT system with constant voltage load.

charge either a GM Chevy Volt EREV or Toyota Motor Company RAV4 EV that is standard at 10-kW power charging. Input power requirements from a standard 220 $V_{\rm ac}$ utility connection, and accounting for WPT losses, result in a design based on 60 A service.

III. Primary-Side Power Control

It is well known that power transmission from an ac voltage source, through a line inductance, and into a rectified dc load at constant potential is severely limited by the series inductance [54]. This situation becomes particularly problematic at the operating frequency of high-power wireless chargers. WPT, at its most basic level, can be viewed as an ac source voltage driving power through a series inductance to a rectified load consisting of a constant potential—the vehicle high energy storage battery of its ESS. Fig. 4 shows the fundamentals of power transmission into a rectified dc constant voltage load. The parameter values given are consistent with the specifications listed in Table I for the ORNL WPT system. In the analysis, the battery voltage is chosen to reflect a nominal EV high-voltage lithium-ion battery pack voltage under charge while its at midrange SOC value. The specific source voltage was taken to be representative of the coupler secondary-side open circuit potential. Secondary coil leakage inductance, L_{ls}, as shown is a realistic value for a 10-kW WPT (note: secondary current I_s must be forced through the full secondary inductance, regardless of coupling coefficient, such as $k \sim 0.24$ representative of a nominal EV ground clearance of 150–160 mm). In the analysis to follow the source frequency, $f = 23\,500$ Hz, consistent with the operating frequency selected by ORNL for WPT charging of EVs based on a silicon thyristor power inverter. Fig. 4 is representative of the WPT secondary over a half period into a full-wave bridge rectifier.

The cut-in angle, β_b, in Fig. 4 occurs when the source voltage U_{s2} exceeds the battery potential U_b, given as (1). Source current is derived as discussed in [54] and repeated here for reference. Peak value of source current $I_s(\beta)$ according to (2) occurs when $\beta = \beta_p$ given in (4) based on the symmetry of the sinusoidal U_{s2} intercepts with U_b. Note that β_p occurs at the negative slope of U_s when it intercepts U_b at which point the line current I_s reaches its peak value

$$\beta_b = \sin^{-1}\left(\frac{U_b}{\sqrt{2}U_{s2}}\right) \tag{1}$$

$$I_s(\beta) = K_{\rm is}[\cos(\beta_b) - \cos(\beta)] - K_{\rm ib}[\beta - \beta_b] \tag{2}$$

where the coefficients $K_{\rm is}$ and $K_{\rm ib}$ are defined according to (3)

$$K_{\rm is} = \frac{\sqrt{2}U_{s2}}{\omega L_{ls}};\ K_{\rm ib} = \frac{U_b}{\omega L_{ls}};\ \rho = \frac{K_{\rm ib}}{K_{\rm is}} = \frac{U_b}{\sqrt{2}U_{s2}} \tag{3}$$

$$\beta_p = \pi - \beta_b. \tag{4}$$

Calculation of the angle, β_f, when $I_s(\beta) = 0$ in the interval $(\pi/2 < \beta < 3\pi/2)$ is found from (2) and given as (5) that must be solved as a transcendental equation

$$\cos(\beta_f) + \rho\beta_f = \rho\beta_b + \cos(\beta_b). \tag{5}$$

Fig. 5 shows the calculated current flow from source U_{s2} into the rectifier and battery for various source potentials. Note that the line current $I_s(\beta)$ is extremely amplitude limited

TABLE II
POWER TRANSFER THROUGH UNCOMPENSATED LINE REACTANCE

U_{s2} (V_{rms})	280	320	360	400	440
I_p (A_{pk})	0.698	3.72	7.72	12.36	17.2
I_d (A_{avg})	0.137	1.244	3.207	5.813	8.916
P_0 (W)	51	460	1187	2151	3299

by the uncompensated secondary inductance of the coupler. At a source potential of 440 $V_{\rm rms}$, the system is only capable of 17.2 $A_{\rm pk}$ into the battery load via a full-wave rectifier and capacitor filter. The charging power, $P_o = U_b{*}I_d$, can be found after computing the average value of the line current $I_s(\beta)$ according to (6). At issue here is derivation of the discontinuous conduction extinction angle, β_f

$$I_d = \frac{1}{\pi}\int_{\beta_b}^{\beta_f}\{I_s(\beta)\}d\beta$$
$$I_d = \frac{K_{\rm is}}{\pi}[(\beta_f-\beta_b)\cos(\beta_b)-\sin(\beta_f)+\sin(\beta_b)] - \frac{K_{\rm ib}}{\pi}\left[\frac{\beta_f^2}{2}+\frac{\beta_b^2}{2}+\beta_f\beta_b\right]. \quad (6)$$

For the series of line current traces shown in Fig. 5, the peak current, average dc output current, I_d, and output power into the constant voltage battery load are summarized in Table II, where the dc current was found by solving (6) as transcendental equation.

In order to develop the open circuit voltage $U_{s2} = 440V_{\rm rms}$ in the WPT secondary a very substantial primary magnetizing current, I_p, as given by (7) will be necessary. In (7), and for the parameter values specified in Table I, with $k_z = 0.24$, $I_p = 93$ $A_{\rm rms}$ is necessary at $f = 23.5$ kHz. This is substantial voltage (and primary current) for such low throughput power, hence the motivation to employ capacitive compensation in the secondary, as shown in Fig. 3. The limitation of sourcing power through uncompensated line reactance is what motivated the shift to using tuned circuits, often termed magnetic resonance couplers

$$U_{s2} = j\omega M I_p = j\omega k_z L_p I_p = 400V_{\rm rms}. \quad (7)$$

The primary source (i.e., HF power inverter) of a WPT system develops the driving point (i.e., source) voltage, U_s, given by (8) that provides primary coil excitation current $I_{\rm pri}$, through a series LC-tuned circuit that includes the magnetizing branch. It should be noted that secondary potential, U_{s2}, is the voltage induced within the secondary winding by the HF flux coupled from the primary coil. This potential, therefore, sources secondary current, I_s, that must flow through the full secondary inductance, L_s. Therefore, high values of secondary inductance are not desirable. Based on the earlier work at ORNL the duty ratio, d, has now been maintained constant at $d = 0.8$ to minimize primary reactive power demand [13] on the HF inverter. Lower values of duty ratio lead to progressively high reactive power at the primary. A tripling of coupler reactive power at half the duty cycle (i.e., $d = 0.4$) is validated in [13, Table II]; this in turn necessitated tripling of the HF inverter dc-link voltage in order to sustain constant throughput power

$$U_s = \frac{2\sqrt{2}}{\pi}U_{d0}\sin\left(d\frac{\pi}{2}\right)\cos(\omega t)(V_{\rm rms}). \quad (8)$$

For the S–P-tuned WPT system the undamped natural frequency, ω_0, given as (9), is shifted to a somewhat higher frequency due to its inherent loose coupling; that is $0.15 < k_z < 0.4$ in general as given by (10). After compensating both primary and secondary with tuning capacitors, C, selected to resonant at a specific frequency within one of the allocated WPT charging bands, in this paper, $f_0 = 22$ kHz. Inputting these values into (9) yields a value for capacitance, $C = 0.43$ μF. However, when the coupler operates over a gap $z = 160$ mm this frequency shifts upward to $f_H = 25.2$ kHz according to (10). The geometric mean of f_0 and f_H is 23.5 kHz. It will be proven later that maximum power in fact transfers at the shifted resonant condition, and furthermore, that a 180° phase shift occurs in the primary, or input, reactance above the higher resonant point

$$\omega_0 = \frac{1}{\sqrt{L_p C}} \quad (9)$$
$$\omega_H = \frac{\omega_0}{\sqrt{1-k_z}}. \quad (10)$$

Fig. 6 shows the basic secondary configuration of S–P-tuned WPT for which the capacitive element appears in parallel with the full-wave rectifier input. The operation is very similar to that given in Fig. 4, and the load current flows when rectifier input voltage, U_r, matches the constant voltage battery load voltage, U_b. This current peaks when the rectifier input voltage just crosses the battery potential during the negative slope of U_r, as shown in Fig. 4 at conduction angle β_p. The secondary-side rectifier input power factor, $\rm PF_s$ is, therefore, always lagging by an amount dictated by the current I_r, cut-in angle, β_b (11). The architecture shown in Fig. 6 has key aspects of static VAR compensation of a utility distribution network that provides voltage support at the load end of a long line, i.e., a high reactance line

$$\mathrm{PF}_s = \cos(\beta_b) = \cos(\pi-\beta_b) = \cos(\beta_p). \quad (11)$$

Prior to current $I_s(\beta)$ cut-in in Fig. 5, the capacitor current, I_c, will flow around the secondary loop with a magnitude dependent on the source frequency relative to the tuning criteria (12). The complimentary secondary rectifier input voltage, U_r, for the current given by (12) is computed according to (13)

$$I_c = \frac{-j\omega C U_{s2}}{\left[\left(\frac{\omega}{\omega_H}\right)^2-1\right]} \quad \forall\sqrt{2}U_{s2} < U_b \quad (12)$$

$$U_r = \frac{-U_{s2}}{\left[\left(\frac{\omega}{\omega_H}\right)^2-1\right]} \quad \forall\sqrt{2}U_{s2} < U_b. \quad (13)$$

Fig. 7 plots the capacitor current for the condition given in (12). Note that the secondary current has leading power factor relative to the rectifier input ac equivalent voltage U_{s2}

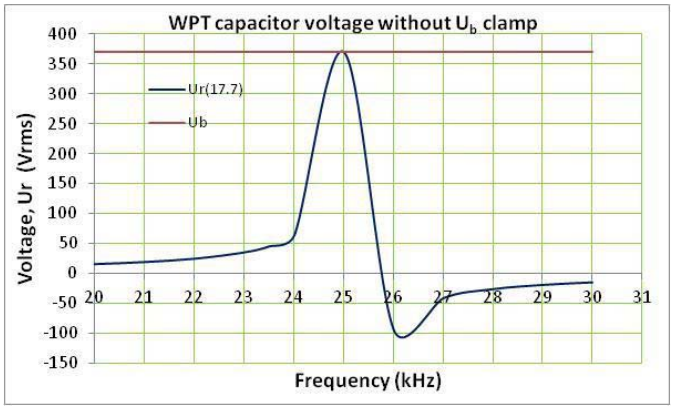

Fig. 7. Compensated secondary and rectifier input voltage matched by $I_c = 17.7\ A_{\rm rms}$.

until the operating frequency exceeds f_H. Furthermore, a very low magnitude of secondary source voltage, $U_{s2} = 4.25\ V_{\rm rms}$ is needed to produce $U_{\rm rpk} = 370$ V owing to a secondary loop current, $I_s = I_c = 17.7\ A_{\rm rms}$. This is the great benefit of designing with tuned circuits for wireless charging; resonant currents of very high magnitude may be readily generated. In this case, the resonant current peaks align with the secondary tuning condition. Two characteristics of WPT secondary-side behavior are apparent in Fig. 7. First, a very low value of secondary source voltage, U_{s2}, develops a high level of secondary-side current and this in turn generates substantial voltage at the rectifier input. Second, during power transfer when the full-wave rectifier diodes impose $+/-U_b$ limits at the input, U_r, the amount of capacitor VA reactive power injection is substantial. Consider the case at hand where $I_c = 17.7\ A_{\rm rms}$ and taking the fundamental rms voltage of the battery load at the rectifier input amounts to significant reactive power

$$Q_{\rm inj} = I_c U_r = I_c \left(\frac{2\sqrt{2}}{\pi} U_b\right) = 5.9\ \text{kVA}. \tag{14}$$

The concept of secondary-side reactive power injection plays a central role in the analysis of WPT performance when the parallel resonant secondary is loaded with a constant voltage source (advanced chemistry battery, such as lithium ion) via a full-wave rectifier. Sections III-A–III-C cover this analysis in depth.

A. WPT Secondary-Side Analysis

Power transmission through the vehicle-mounted secondary coil, tuning components, and power conversion electronics are developed in this section with reference to the waveform in Fig. 4 and equivalent circuit of Fig. 5. The analysis to follow is an extension of the work started in [8]. According to the waveforms shown in Fig. 4, the load current into a constant voltage load has a cut-in angle, β_b, having a unique relationship to the point at which the capacitor voltage at the rectifier input, U_r, breaks over the load voltage, U_b. Research and experimental work have shown that $\beta_b > 1$ radian has very low occurrence, as does $\beta_b, \rightarrow 0$ radian. Therefore, in this paper, the analysis is based on a break-over value $\beta_b = 0.5$ radian as an average condition; consequently, we define the resulting duty ratio, D, of rectifier input current, I_r, according to (15). Using this value of duty cycle, the equivalent ac value of U_r is determined according to (16)

$$D = \left(1 - \frac{2\beta_b}{\pi}\right) \qquad (\#) \tag{15}$$

$$U_r = \sqrt{1 - \frac{2\beta_b}{\pi}}\, U_b \qquad (V_{\rm rms}). \tag{16}$$

Given that desired output power, P_o, be delivered to the battery having potential, U_b, via load current, I_d, requires that an equivalent ac value of rectifier input current, I_r, and reactive power injection via I_c be as follows:

$$I_r = \frac{P_o}{\eta_r U_r \cos(\beta_b)} \tag{17}$$

$$I_d = \frac{P_o}{U_b} \tag{18}$$

$$I_c = j\omega C U_r = j\omega C \sqrt{D} U_b \tag{19}$$

where an average efficiency value, η_r, of the load-side rectifier is included in (17) so that input ac parameters will have representative real-world magnitudes. It is also evident that for $U_b = 370\ V_{\rm dc}$ that leading reactive power injected by the resonant capacitor, C, given by (19) will be on the order of that given in (14). Secondary ac current, I_s, is the vector sum of capacitor current and rectifier input current according to (20), noting that rectifier input current I_r lags U_r, whereas I_c leads U_r by 90°, given that $U_r = |U_r| \angle 0°$ is taken as the reference. In the analysis that follows, the variables stated in (16) and thereafter are approximated as sinusoidal so that phasor notation may be used to simplify calculations and offer greater insights.

$$I_r \angle \beta = a_r - j b_r \qquad I_c \angle \frac{\pi}{2} = j b_c \tag{20}$$

$$I_s \angle \theta_s = a_r + j(b_c - b_r) \tag{21}$$

$$\theta_s = \tan^{-1}\left[\frac{(b_c - b_r)}{a_r}\right]. \tag{22}$$

The reader is forewarned that computation of angles be carried out with care, as the ranges of validity of trigonometric quantities are sensitive to which quadrant the argument falls into, and to note that impedances are complex numbers, not phasors. Having made this point, the next computation according to Fig. 4 is the one of impedance, the secondary-side leakage inductance, $Z_{ls} = j\omega L_{ls}$, for which secondary coil ac resistance, $R_{\rm ac}$, is negligible in comparison. For a given secondary ac current, I_s, and line impedance, the secondary coil internal-induced voltage, U_{s2}, will be computed (24) following the determination of the line reactance voltage drop (23). It is again important to recognize the equivalence made of WPT secondary power transmission with that of a utility grid, or microgrid, line reactance and voltage model in which the secondary tuning capacitor acts as a static VAR compensator on a utility network to improve voltage regulation

$$U_{ls} \angle \theta_{ls} = Z_{ls} I_s = a_{Uls} + j b_{Uls}. \tag{23}$$

TABLE III
COMPUTED AND MEASURED VARIABLES FOR WPT COUPLER AT $P_o = 3.3$ kW INTO $U_b = 370$ V_{dc} (MEANS INACCESSIBLE)

Variable	U_r (16) (V_{rms})	Z_{ls} (Ω)	I_r (17) (A_{rms})	I_d (18) (A_{dc})	I_c (19) (A_{rms})	I_s (21) (A_{rms})	U_{ls} (23) (V_{rms})	U_{s2} (24) (V_{rms})	I_m (25) (A_{rms})	I_p (24) (A_{rms})
Cal	305	j12.3	12.7	8.92	19.4	17.4	216.2	197.5	37.5	42.9
Meas	305	-		9		25.4	-	-	-	42.4

Therefore, following the methodology of (21), the secondary induced voltage, U_{s2}, is computed as the vector sum of (16) and (23) given as:

$$U_{s2}\angle\theta_{s2} = (U_r + a_{Uls}) + jb_{Uls}. \tag{24}$$

Before proceeding with WPT primary-side analysis, there are two tasks remaining: 1) determination of the coupler (at $z =$ specified gap) magnetizing current, I_m, and 2) determination of the value of primary current, I_p, required to support the stated load power. Computation of the magnetizing branch voltage, U_{s2}, that is the voltage across the magnetizing flux of the coupler, to match (24), determines the effective magnetizing current, I_m, according to (25), found by expanding on (7)

$$I_m\angle\theta_m = \frac{U_{s2}\angle\theta_{s2}}{j\omega M} = \frac{U_{s2}\angle\theta_{s2}}{j\omega k_z L_{\text{pri}}}. \tag{25}$$

By convention phasor rotation is counterclockwise that means the angle in (25) will be shifted 90° clockwise by the angle of the magnetizing impedance. Therefore, and since secondary-side ac current I_s is known, the primary current is calculated from phasor analysis of (25) using (21) resulting in

$$I_p\angle\gamma = I_m\angle\theta_m - I_s\angle\theta_s. \tag{26}$$

As (26) makes clear, the net primary current is the resultant of Lenz's law operating on the coupler magnetizing flux (i.e., in opposition) so that as loading increases the secondary current follows suit and in order to sustain the requisite magnetizing current the primary current must increase proportionally. It is instructive to point out that although the WPT coupler may be referred to as a loosely coupled transformer, in reality, this is less accurate than saying that it is a magnetic resonance coupler and by the same merit turns ratio begins to lose meaning as the coupling coefficient, $k_z \to 0$. This is the case, since in a real transformer, such as the HF isolation and matching transformer shown in Fig. 3, the coefficient of coupling $k_z \to 1$.

This section concludes with an illustration of the procedure of the analysis given above for the coupler secondary according to Fig. 5 for the values given in Table I and for an output power $P_o = 3.3$ kW into battery emulator load, $U_b = 370$ V_{dc}. The phasor diagram of Fig. 8 shows the key WPT variables discussed to this point.

Table III summarizes the computed values for the WPT coupler secondary variables as calculated from (15) through (26) and shown in comparison with laboratory measurements taken on the coil that is specified in Table I.

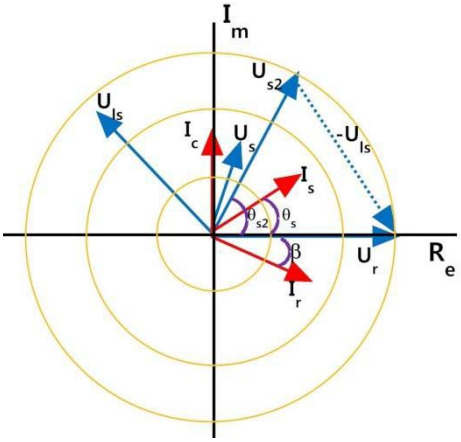

Fig. 8. Phasor diagram showing secondary-side variables when $U_b = 370$ V_{dc} and $P_o = 3.3$ kW.

Measurements are made in the laboratory using a power analyzer with voltage isolation probes and either commercial current transducers or industrial current sensors. As noted in the table, some variables remain inaccessible and some are not being monitored, only calculated.

To reinforce the point made about treating the WPT secondary as a utility transmission line with VAR compensator the power throughput magnitudes are computed for reference using the data in Table III. Real power (27) is that power which can be forced through a line reactance having generating voltage source, U_{s2}, and load voltage under regulation, U_r. Real power transfer is strongly dependent on the line reactance. Similarly for reactive power (28) and (29), the magnitude is determined by the line reactance and partially compensated for by the VAR injection of the secondary-side capacitor (29)

$$P_o = \frac{U_{s2}U_r}{\omega L_{ls}}\sin(\delta) = \frac{197.5(305)\sin(0.784)}{0.138(1-k_z)122} = 3604(W) \tag{27}$$

$$Q_{s2} = \frac{U_{s2}^2}{\omega L_{ls}} - \frac{U_{s2}U_r}{\omega L_{ls}}\cos(\delta) = \frac{197.5^2}{11.8} - \frac{197.5(305)}{11.8}\cos(0.784) = -309 \text{ (VA)} \tag{28}$$

$$Q_{\text{inj}} = I_c U_r = 19.4(305) = 5917 \text{ (VA)}. \tag{29}$$

For the real and reactive secondary power, the secondary power factor can be computed according to (30) by considering the injected leading VARs when $f = 22$ kHz. Note also that the natural frequency of the secondary-side LC, given that

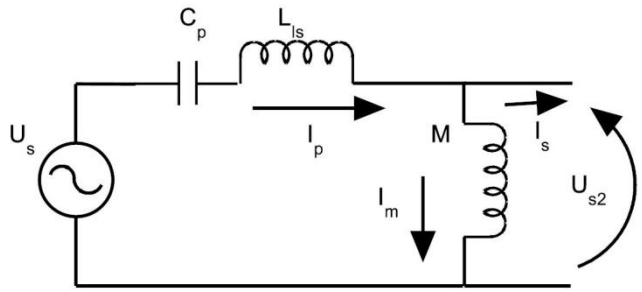

Fig. 9. WPT series-tuned primary and secondary-side driving voltage U_{s2}.

$C = 440$ nF, is $f_o = 21.7$ kHz

$$\mathrm{PF}_s = \cos\left\{\tan^{-1}\left(\frac{Q_{s2}+Q_{\mathrm{inj}}}{P_o}\right)\right\} = \cos\left\{\tan^{-1}\left(\frac{5917-309}{3604}\right)\right\} = 0.54. \quad (30)$$

The value computed for secondary-side power factor is in good agreement with test data taken using the ORNL 5-kW WPT hardware, and as stated in (30), it is a leading PF. Moreover, as primary current increases, the power transmission will increase in direct proportion since the induced voltage within the secondary coil, U_{s2}, increases linearly with current at a given coupling coefficient. This means that as drive power increases, so will the output power (27), but the secondary reactive power (28) will only increase slightly, while injected power will remain relatively constant. Therefore, and according to (30), the secondary-side power factor will improve with the increasing output power.

B. WPT Primary-Side Analysis

Attention now turns to the primary side of the WPT system shown schematically in Fig. 9 and consisting of the series-tuned compensation of leakage inductance and magnetizing branch. Application of source voltage, U_s, using (8) by the HF power inverter having duty ratio, $d = 0.8$, gives rise to primary current, I_p, that magnetizes the air between primary and secondary coils of the coupler. The fundamental requirement of magnetic resonance power transfer is that sufficient current must flow in the primary of the coupler to establish sufficient flux in the secondary that will in turn deliver a specified amount of power. This current, shown as magnetizing branch current I_m in Fig. 9, provides the primary with a sufficient magnetic dipole moment to generate the mutual flux needed by the secondary. From Section III-A, the requisite electromotive force (shown as U_{s2} in Fig. 9) and primary current have been computed. The task at hand is to determine the magnitude of the source, or driving point, voltage U_s necessary to transfer this amount of current.

The WPT system has been intentionally cast as a utility transmission line equivalent secondary and with the primary side under consideration here as providing the frequency selectivity stage, much the same manner as a low-noise amplifier in a radio effects station selection. This function is performed via a high-Q-tuned circuit, an LC circuit in Fig. 9, that compensates the coupler's high input leakage inductance so that a reasonable value of source voltage, U_s, can readily provide sufficient primary current to magnetize the working gap. The practical implications of sustained high current at high frequencies are provided by the citations listed in Section I-C.

Input frequency selectivity of the WPT system is derived as (31), where the HF inverter angular frequency, ω, is normalized by the natural frequency of tuning, ω_o, given as (10) but written explicitly in terms of coupling coefficient for clarity

$$Z_p = \frac{j}{\omega C_p}\left[(1-k_z)\left(\frac{\omega}{\omega_0}\right)^2 - 1\right] \quad (31)$$

$$U_s\angle\varphi = U_{s2}\angle\theta_{s2} + Z_p I_p \angle\gamma\,(V_{\mathrm{rms}}). \quad (32)$$

Source voltage U_s is, therefore, the vector sum of the voltage developed across the air gap, U_{s2}, and the primary-side leakage inductance Z_p, and its magnitude as modified by the location of source frequency relative to its natural frequency. Note too that when the source angular frequency, ω, lies below the upper (i.e., shifted) natural frequency, ω_H, of (10) that the argument of Z_p is lagging, whereas when the input angular frequency, ω, lies $>\omega_H$ the argument of Z_p is leading. This is the phenomena whereby the input power factor of the WPT system makes a sharp reversal, and as will be seen in the experimental data, it occurs at a point that also depends on the argument of the primary current due to secondary loading.

To conclude this section on WPT primary-side analysis, (8) will be solved for HF inverter dc rail voltage, U_{d0}, and by doing, so the mechanism of primary-side power regulation will be realized

$$U_{d0} = \frac{\pi\,|U_s|}{2\sqrt{2}\sin\left(d\frac{\pi}{2}\right)}. \quad (33)$$

Voltage U_{d0} is the dc rail voltage that appears at the output of the AFE shown in Fig. 3 having magnitude calculated in (33) that can be manipulated by the AFE's power factor corrector voltage loop according to its controller algorithm. In a similar manner, the HF power inverter stage center frequency, or operating frequency, f, is set by this same controller, and manipulated in specific incremental steps in response to secondary-side power flow so that gap variations can be accommodated in (27) and (33). Note that in (27), we have $L_{ls} = (1-k_z)L_s$, a factor in secondary-side power transmission.

C. Model and Simulation of WPT Power Transfer

The WPT coupler shown in Fig. 10 was designed for integration into an aftermarket PRIUS plug-in hybrid for charging at 5-kW power level. The primary and secondary are identical in size and wound with #6 AWG Litz cable having 50-kHz bandwidth. Simulation results of the model described in Sections III-A and III-B are shown in Figs. 11 and 12 for output power and primary current under ideal conditions, respectivly, (resistances neglected). Note the use of square geometry windings to accommodate low-cost flat ferrite plates as the flux guides. An aluminum backing plate is used for

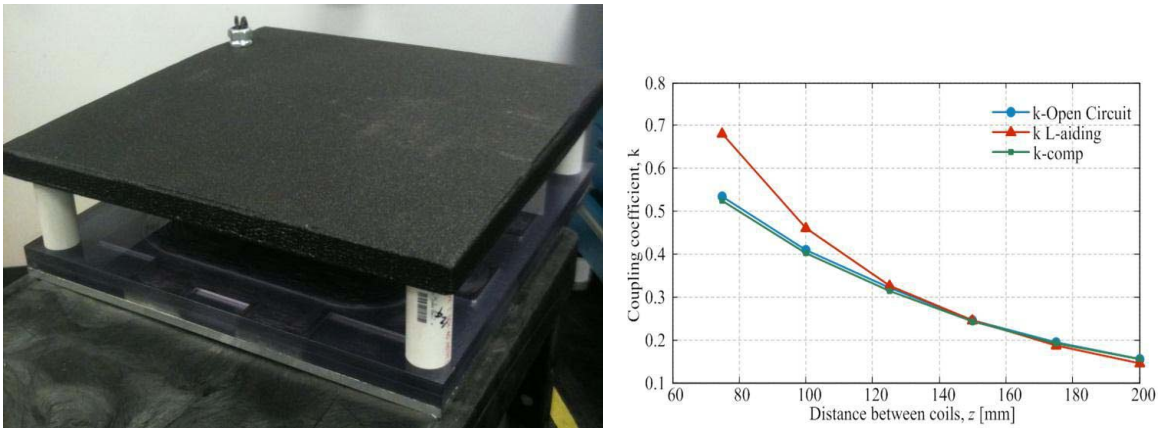

Fig. 10. WPT coupler (specifications in Table II) used for simulation and its characterized coupling coefficient, k_z [5].

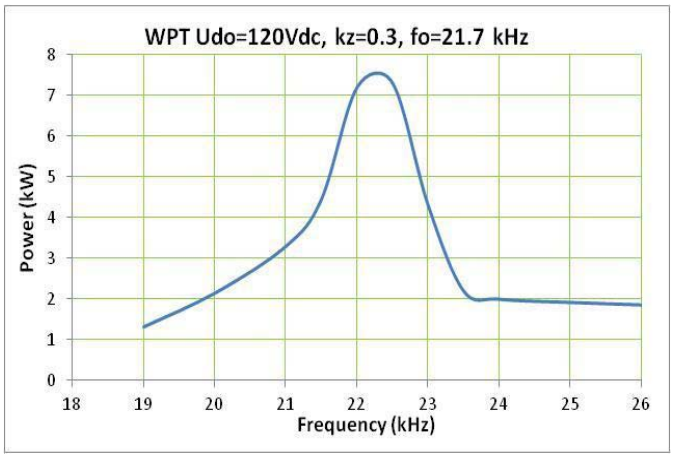

Fig. 11. WPT power transmission as function of input frequency.

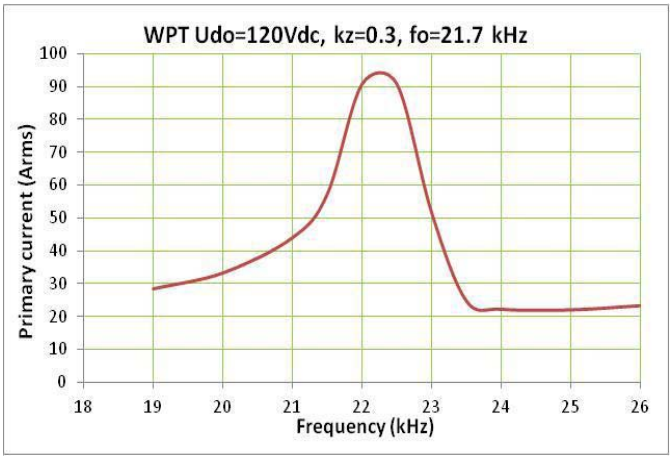

Fig. 12. WPT primary coil current under ideal conditions.

both structure and electromagnetic field shielding. This coupler design and its leakage field characteristics are the topic of a separate paper.

Fig. 11 shows model calculated power transfer into a $U_b = 370\ V_{\rm dc}$ battery emulator for a HF power inverter rail voltage $U_{d0} = 120\ V_{\rm dc}$ and nominal value of coupling coefficient, $k_z = 0.3$. The strongly peaked response of the WPT power transmission is a consequence of holding U_{d0} (33) constant as input angular frequency is varied. There are two important practical considerations to take away from this simulation of the actual hardware. First, the peak of the power transmission curve is right shifted from the tuned point, f_0. Second, the peak power appears to be boosted above its off-resonance magnitude by a factor of ~4 (25 kHz) to ~7 (19 kHz). In some derivations based on resistive loading this boosting is attributed to secondary coil quality, Q. The reader may refer to the text above (9) regarding the value of f_0.

Fig. 12 shows the input current to the coupler primary coil corresponding to the power curve above. It is very apparent that power transmission reflects input current to a high degree of precision. This is transformer action for the case of a highly frequency selective transformer. A further point to make is that this frequency selectivity becomes progressively tighter (i.e., higher Q) the higher the tuned frequency (e.g., 48, 85, and 144 kHz). This point has been developed in depth in a companion paper on the comparison of WPT performance in the four different center frequency bands.

IV. Experimental Results

ORNL's WPT laboratory experimental hardware and controls development are shown in Fig. 13, where the WPT base station power electronics are contained in the NEMA box shown in the center. Power supply and power analyzers, both Yokagawa and Hioki are shown on the power supply. The controller DSP is packaged in the NEMA box along with HF power inverter, gate drivers, signal conditioning, and high-frequency isolation transformer. Also shown in Fig. 13 are the coupling coils with primary coil on the left and secondary coil on the right. The primary coil is fabricated on a 9.5-mm-thick aluminum backing plate for structural rigidity. The pattern of low-loss (3C90 MnZn) ferrite plates used as flux guides shown in the figure are ~160 mm in length, 70 mm in width, and 4.5 mm in thick. The secondary coil is shown conformal coated for mounting beneath a test vehicle (WPT mule vehicle). During testing the coils are stacked, as

Fig. 13. WPT system and laboratory equipment used in performance testing.

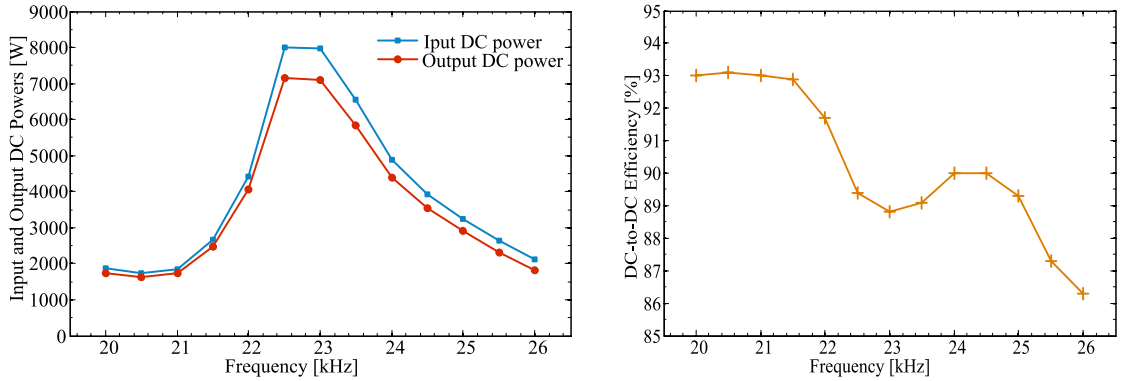

Fig. 14. Experimental results for $P \sim 7$ kW, $U_{\rm do} = 135$ $V_{\rm dc}$, $U_b = 420$ $V_{\rm dc}$, $d = 0.7$, $C_p = 0.44$ μF, and $z = 125$ mm.

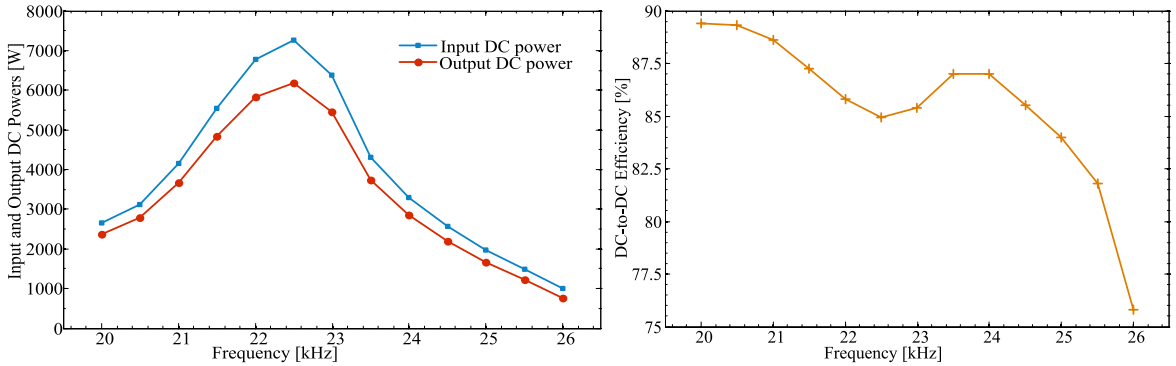

Fig. 15. Experimental results for $P \sim 7$ kW, $U_{\rm do} = 135$ $V_{\rm dc}$, $U_b = 420$ $V_{\rm dc}$, $d = 0.7$, $C_p = 0.44$ μF, and $z = 150$ mm.

shown in Fig. 10, as they would be in a field installation. The spacers are used to preset the physical gap between the coils.

The experimental hardware shown in Fig. 13 was tested at three different gaps between primary and secondary coils in the coupler for comparison with model and simulation results discussed in Section III-C, but with some parameter variations. In these tests, the coupler is set for fully aligned conditions: no tilt, and no offset. The experimental tests are done with the power supply set at 135 $V_{\rm dc}$, the HF power inverter duty, $d = 0.7$, and the load voltage is 420 $V_{\rm dc}$. Although slightly different from the modeled results of Section III-C, the intention here is to show the differences in power transfer band shape versus frequency for real-world conditions that will arise based on how the primary coil is placed, whether on the floor or embedded into the floor (i.e., changes gap, z) and the influence of vehicle battery pack voltage that will occur depending on its SOC. Reducing the inverter duty below that used in the model and simulation (i.e., $d = 0.8$) requires a corresponding increase in its dc rail voltage, $U_{\rm do}$ (33). The key point is that variation of physical and electrical variables introduces noticeable shape differences in the power transfer function, $P_o(f)$, as shown in the following sequence of plots. Most evident is the shift in power-transfer peak to lower frequency as gap increases. In addition, apparent is the dip in efficiency at peak power due to the higher currents in the coupler and electronics (Fig. 12). Figs. 14–16 show $P_o(f)$ at the inverter and load, and overall dc–dc efficiency.

Experimental voltage and current waveforms at both primary and secondary side are shown in Fig. 17 for the same conditions listed in Fig. 14, but taken for $f = 23$ kHz at peak

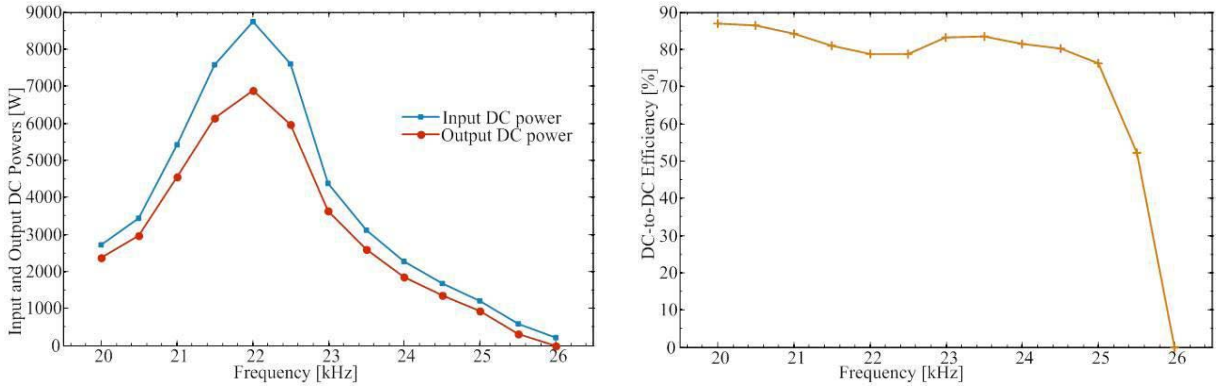

Fig. 16. Experimental results for $P \sim 7$ kW, $U_{\rm do} = 135\ V_{\rm dc}$, $U_b = 420\ V_{\rm dc}$, $d = 0.7$, $C_p = 0.44\ \mu$F, and $z = 175$ mm.

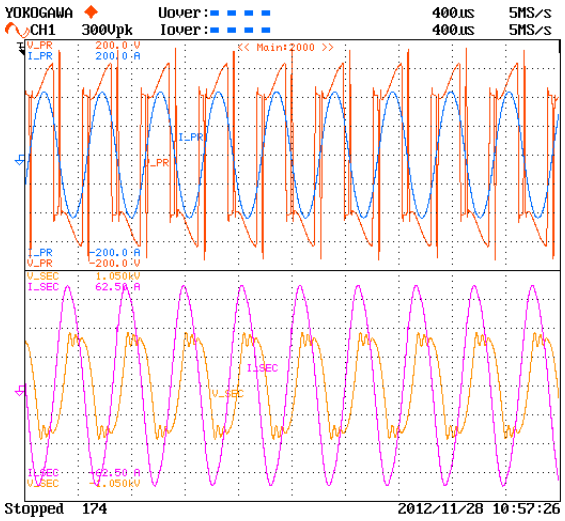

Fig. 17. Experimental waveforms corresponding to Fig. 14, all currents are sinusoidal, $f = 23$ kHz. Top: HF inverter voltage and current. Bottom: secondary coil voltage and current.

power, the region for which input power factor is approaching unity. HF power inverter antiparallel diode switching points are also clear in the upper trace voltage waveform, as is the secondary-side rectifier diode switching-induced ringing on the load voltage-clamped secondary voltage waveform.

Fig. 17 also shows clearly the clipped voltage at the secondary when the tuning capacitor voltage intersects the switching points of the full-bridge rectifier with constant voltage load, in this case $U_b = 420\ V_{\rm dc}$. During rectifier diode turn ON, there is parasitic inductance in the circuit resulting in the damped oscillation at ~83 kHz. Note also that secondary current (sinusoidal) leads the clipped capacitor voltage in agreement with reactive power injection conjecture made in Section III-A.

V. Practical Considerations

The field of wireless, or noncontact, power transfer for charging of electric vehicles is currently undergoing dramatic changes in design activities worldwide on coupler type, center frequency, and vehicle mounting locations. Add to this list what the practical requirements are, such as tolerance to misalignment, effect of magnetic gap on operating frequency, and how any combination of these impacts leakage fields. Sections V-A–V-C focus on each of these key areas and include experimental results obtained at ORNL's WPT laboratory.

A. Coupler Misalignment Tolerance

The coupler shown in Fig. 10 has relatively square coils (Fig. 13) is amenable to a quick assessment of offset by simply shifting the secondary plate relative to the primary in either x-axis, or y-axis, or a combination. Misalignment is defined as the percentage nonoverlap area relative to the primary coil area. For example, a 20% misalignment would mean $\Delta x/x = 0.2$ and so on. It has been found experimentally that misalignment has the same effect on power transmission in WPT as increasing the magnetic gap. In these tests, the frequency is held constant at a nominal $f = 23$-kHz representing peak power. During these misalignment tests, the HF power inverter frequency was not adjusted and this mistuning accounts for the increased input and throughput power going from fully aligned (100%) to 10% misaligned x-axis. When both x-axis and y-axis are misaligned, and for the same inverter conditions, the primary apparent power decreases resulting in the drop in real power with complimentary increase in primary reactive power, as shown in Fig. 18.

B. Magnetic Gap Influence on Frequency

The effect of magnetic gap on frequency has been alluded to in the sequence of Figs. 14–16. Fig. 19 summarizes the effects of gap variation on power transmission, $P_o(f)$, during this testing, the HF power inverter rail voltage is adjusted to hold uniform peak output power of $P_o = 5$ kW. The experimental data shows that the coupler exhibits $\sim\Delta f/f_o = -1.7$ % for $z = 150$ mm–25 mm, and $\Delta f/f_o = +2.75$ % for $z = 150$ mm + 25 mm, where $f_o = 23.5$ kHz. This nonlinear variation of frequency shift with gap must be accommodated in the WPT controller algorithm that adjusts HF inverter frequency to track peak power transmission. The fact that $P_o(f)$ shape varies with magnetic gap and power level has already been pointed out.

C. Leakage Fields

High-frequency magnetic and electric field emissions from wireless charging are the most pressing concerns for

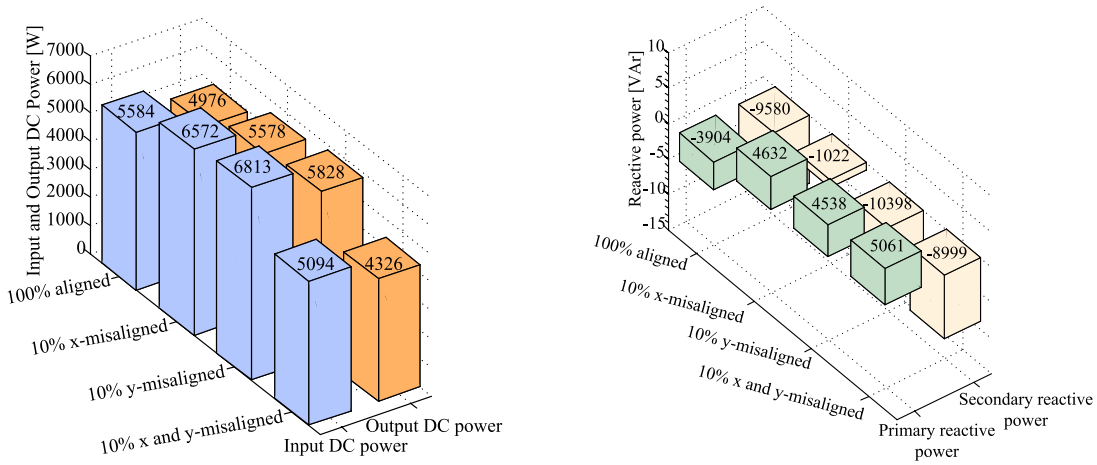

Fig. 18. Experimental validation of coupler misalignment for $z = 125$ mm. Left: input and output dc power. Right: input and output reactive power.

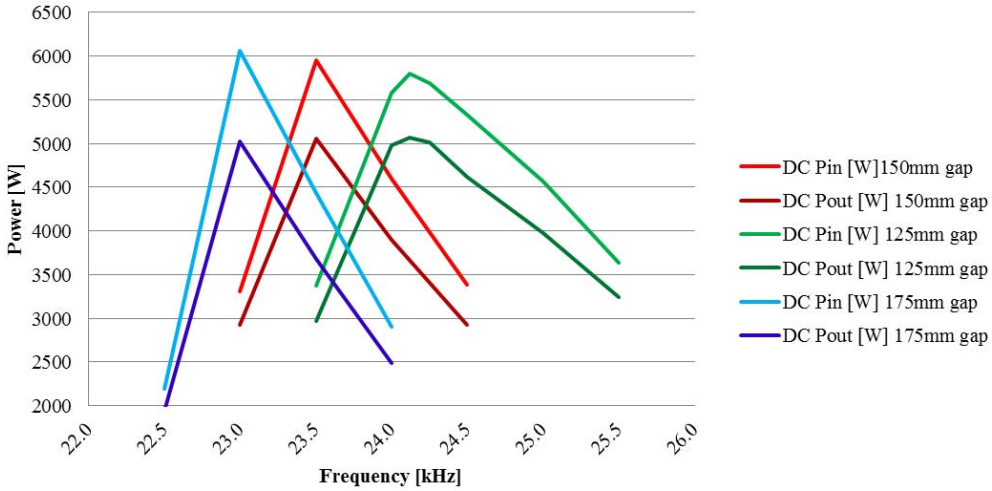

Fig. 19. Experimental validation of gap variation on $P(f)$.

this technology. By its nature, a WPT charger must develop a magnetic field between primary and secondary coils for the purpose of facilitating power transmission. The degree to which this magnetic coupling field can be confined is strongly dependent on coupler design, particularly, on the type and placement of ferrite flux guides and on the material and shape of any shielding plates used (shield plate is aluminum since sheet steel would incur high losses). The coupler evaluated in the ORNL work is fabricated with thin ferrite plates and a flat aluminum back plate (as well as shallow aluminum trays) for both structure and shielding. Ongoing work in coupler design at ORNL in which somewhat thicker ferrite was employed ($\sim$10 mm) and more significantly where the aluminum shield was formed into a pan with flange sides extending somewhat beyond the ferrite thickness the leakage fields were very low, on the order of 15% of those discussed in this section. Coupler design has very strong electromagnetic criteria that must be met in order to develop the highest coupling coefficient.

Fig. 20 shows the placement of a NARDA EH50D electromagnetic field analyzer relative to the coupler centerline. The coupler primary sits on a concrete floor as it would in a residential wireless charging application. The influence of concrete floor reinforcement rod and/or wire mesh is beyond the scope of this paper and left for future research

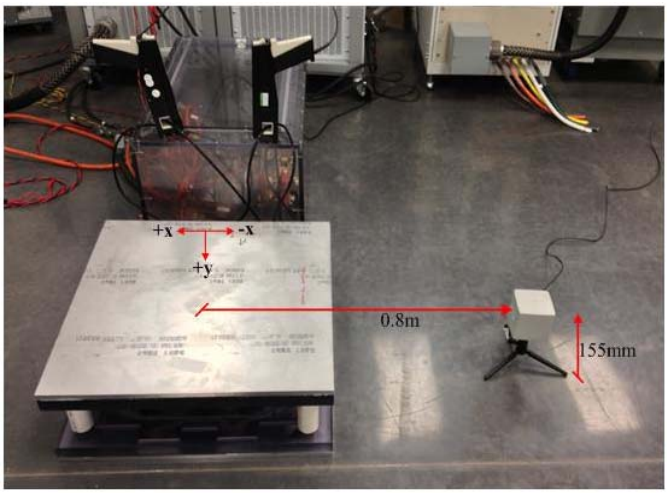

Fig. 20. Experimental configuration for leakage fields. Test conditions: $U_b = 370$ $V_{\rm dc}$, $d = 0.8$, $P_o = 5$ kW, and $z = 150$ mm.

on high-frequency magnetic and electric field emissions, such as ground wave propagation.

Criteria for leakage fields are that magnetic field maximum permissible exposure (MPE) levels are restricted to lie below internationally specified values. Discussion on how MPEs are

TABLE IV
MEASURED LEAKAGE FIELDS FOR COUPLER AT $P_o = 3.3$ kW, $f = 22$ kHz, and $z = 125$ mm

Coupler alignment	Magnetic field	Electric field
	(μT)	(V/m)
Fully aligned	2.9	56.6
10% misaligned	7.2	63.5

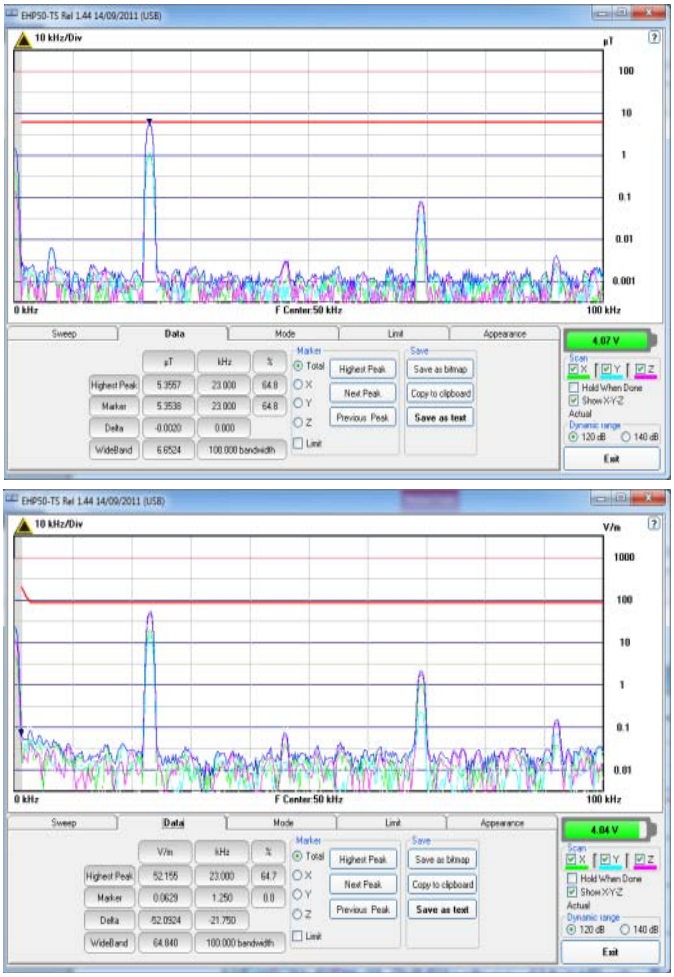

Fig. 21. Measured magnetic and electric fields at field point ($x = 0.8$ m and $z = 0.155$ m) in 40 Hz $< f <$ 100 kHz. (a) B-field fundamental peak 5.387 μT. (b) E-field fundamental peak 52.155 V/m.

derived is outside the scope of this paper but for WPT in the 10–148-kHz band $|B| < 6.25$ μT, and $|E| < 87$ V/m. The leakage fields measured at the field point shown in Fig. 20 for 5-kW power transfer fall well within these criteria. It must be mentioned here that leakage fields increase with increasing magnetic gap and for increasing misalignment. In addition, and as will be developed in a companion paper, the maximum B- and E-fields are not necessarily collocated.

In a separate, but related test, at a power level of 3.3 kW to the battery emulator and for a coupler gap of 125 mm, the leakage fields measured are summarized in Table IV.

In this second test of leakage field, the output power has been decreased by ∼33% (3.3 versus 5 kW) and the B-field is reduced by 46% (2.9 versus 5.387 μT), whereas the electric field is nearly the same. This is most likely due to a somewhat different placement of the NARDA field sensor. Similar E-field behavior is evident from the fact that B-field magnitude increases by 248% for 10% misalignment but the E-field increases only 12%. Examination of Fig. 21 shows that the harmonic content of the E-field is different from the B-field. This is due in part to how the primary coil is being driven, whether single-ended drive or balanced drive (the ORNL primary is single-ended drive), and to the fact that the B- and E-fields are spatial and temporal derivatives of the coupling field magnetic vector potential, respectively.

VI. CONCLUSION

This paper summarizes a new analysis process for the computation of wireless charging technology and its performance as documented at the ORNL during the execution of a technology demonstration project funded by the U.S. DOE. The approach taken is novel in that primary-side power regulation is selected and developed with the aim to minimize vehicle on board complexity, size, and cost while retaining key scalability features considered necessary to meet future higher power WPT applications. The specific analysis methodology employed develops beyond the power electronic fundamentals used to compute the electric current flow from an ac source through a line inductance into a fixed dc voltage load, such as a battery, via a diode rectifier. Another unique feature of the ORNL primary-side regulation method is a separate treatment of secondary and primary sides of the magnetic resonance coupler. For the secondary, the analysis parallels that of a utility network or a microgrid in which reactive power compensation is utilized for voltage control, which in a WPT system, is the voltage appearing at the input of the full-wave rectifier. The primary side of the coupler on the other hand is treated as the center frequency selectivity stage needed to insure that a high mutual flux is developed, that in turn facilitates power transmission. In addition to these key aspects of the ORNL approach is the specific treatment of coupler misalignment, variable coupling gap, and leakage field containment all supported with experimental evidence. A thorough compilation of relevant citations are grouped by WPT focus area.

ACKNOWLEDGMENT

The authors would like to thank the members of the Oak Ridge National Laboratory Power Electronics and Electric Machinery Group, especially S. Campbell, C. Coomer, L. Seiber, and C. White, for their contributions to WPT experimental fabrication, testing, and data acquisition. The

authors would also thank the team members D. E. Smith, P. T. Jones, and P. Chambon for their assistance in contract and vehicle systems aspects of this program.

REFERENCES

[1] *Commercial Wireless Chargers: Qualcomm/HaloIPT*. [Online]. Available: http://www.qualcomm.com/solutions/wireless-charging/qualcomm-halo; *Evatran*. [Online]. Available: http://www.pluglesspower.com/; *Witricity*. [Online]. Available: www.witricity.com/; *Momentum Dynamics*. [Online]. Available: www.momentumdynamics.com/, accessed Jan. 30, 2014.

[2] SAE J2954. *Task Force on Wireless Power Charging*. [Online]. Available: http://www.sae.org, accessed Jan. 30, 2014.

[3] M. Pinuela, D. C. Yates, S. Lucyszyn, and P. D. Mitcheson, "Maximizing DC-to-load efficiency for inductive power transfer," *IEEE Trans. Power Electron.*, vol. 28, no. 5, pp. 2437–2447, May 2013.

[4] P. Ning, J. M. Miller, O. C. Onar, C. P. White, and L. D. Marlino, "A compact wireless charging system development," in *Proc. 28th Annu. IEEE Appl. Power Electron. Conf. (APEC)*, Long Beach, CA, USA, Mar. 2013, pp. 3045–3050.

[5] O. C. Onar, J. M. Miller, S. L. Campbell, C. Coomer, C. P. White, and L. E. Seiber, "Oak Ridge National Laboratory wireless power transfer development for sustainable campus initiative," in *Proc. IEEE Transp. Electrification Conf. Expo (ITEC)*, Dearborn, MI, USA, Jun. 2013, pp. 1–8.

[6] N. Y. Kim, K. Y. Kim, J. Choi, and C.-W. Kim, "Adaptive frequency with power-level tracking system for efficient magnetic resonance wireless power transfer," *Electron. Lett.*, vol. 48, no. 8, pp. 452–454, Apr. 2012.

[7] J. M. Miller, "Wireless power charging fundamentals and challenges," in *Proc. SAE Hybrid Veh. Technol. Symp.*, San Diego, CA, USA, Feb. 2012, pp. 1–17.

[8] J. M. Miller and O. C. Onar, "Wireless power transfer systems: Educational short course on wireless charging," in *Proc. IEEE Transp. Electrification Conf. Expo (ITEC)*, Dearborn, MI, USA, Jun. 2013.

[9] C.-Y. Huang, J. T. Boys, and G. A. Covic, "LCL pickup circulating current controller for inductive power transfer systems," *IEEE Trans. Power Electron.*, vol. 28, no. 4, pp. 2081–2093, Apr. 2013.

[10] C.-Y. Huang, J. T. Boys, G. A. Covic, and S. Ren, "LCL pick-up circulating current controller for inductive power transfer systems," in *Proc. IEEE Energy Convers. Congr. Expo. (ECCE)*, Atlanta, GA, USA, Sep. 2010, pp. 640–646.

[11] M. Chinthavali, O. C. Onar, and J. M. Miller, "A wireless power transfer system with active rectification on the receiver side," presented at the *Conf. Electr. Roads Veh. (CERV)*, Park City, UT, USA, Feb. 2013, pp. 1–23.

[12] P. Ning, O. Onar, and J. Miller, "Genetic algorithm based coil system optimization for wireless power charging of electric vehicles," in *Proc. IEEE Transp. Electrification Conf. Expo (ITEC)*, Dearborn, MI, USA, Jun. 2013, pp. 1–5.

[13] J. M. Miller, C. P. White, O. C. Onar, and P. M. Ryan, "Grid side regulation of wireless power charging of plug-in electric vehicles," in *Proc. IEEE Energy Convers. Congr. Expo. (ECCE)*, Raleigh, NC, USA, Sep. 2012, pp. 261–268.

[14] Y.-H. Chao, J.-J. Shieh, C.-T. Pan, W.-C. Shen, and M.-P. Chen, "A primary-side control strategy for series-parallel loosely coupled inductive power transfer systems," in *Proc. 2nd IEEE Conf. Ind. Electron. Appl. (ICIEA)*, Harbin, China, May 2007, pp. 2322–2327.

[15] Y.-H. Chao, J.-J. Shieh, C.-T. Pan, and W.-C. Shen, "A closed-form oriented compensator analysis for series-parallel loosely coupled inductive power transfer systems," in *Proc. IEEE Power Electron. Specialists Conf. (PESC)*, Orlando, FL, USA, Jun. 2007, pp. 1215–1220.

[16] H. L. Li, A. P. Hu, G. A. Covic, and C. Tang, "A new primary power regulation method for contactless power transfer," in *Proc. IEEE Int. Conf. Ind. Technol. (ICIT)*, Gippsland, VIC, Australia, Feb. 2009, pp. 1–5.

[17] B. Sharp and H. Wu, "Asymmetrical voltage-cancellation control for LCL resonant converters in inductive power transfer systems," in *Proc. 27th IEEE Appl. Power Electron. Conf. (APEC)*, Long Beach, CA, USA, Feb. 2012, pp. 661–666.

[18] H. H. Wu, A. Gilchrist, K. Sealy, P. Israelsen, and J. Muhs, "Design of symmetric voltage cancellation control for LCL converters in inductive power transfer systems," in *Proc. IEEE Int. Electr. Mach. Drives Conf. (IEMDC)*, Niagara Falls, NY, USA, May 2011, pp. 866–871.

[19] M. Budhia, G. A. Covic, and J. T. Boys, "Design and optimization of circular magnetic structures for lumped inductive power transfer systems," *IEEE Trans. Power Electron.*, vol. 26, no. 11, pp. 3096–3108, Nov. 2011.

[20] G. A. Covic, M. L. G. Kissin, D. Kacprazak, N. Clausen, and H. Hao, "A bipolar primary pad topology for EV stationary charging and highway power by inductive coupling," in *Proc. IEEE Energy Convers. Congr. Expo. (ECCE)*, Phoenix, AZ, USA, Sep. 2011, pp. 1832–1838.

[21] K. Kobayashi, N. Yoshida, Y. Kamiya, Y. Daisho, and S. Takahashi, "Development of a non-contact rapid charging inductive power supply system for electric-driven vehicles," in *Proc. IEEE Veh. Power Propuls. Conf. (VPPC)*, Lille, France, Sep. 2010, pp. 1–6.

[22] S. Mao, R. Lu, C. Su, and C. Zhu, "Frequency characteristic of resonance-based wireless energy transfer," in *Proc. 16th Int. Symp. Electromagn. Launch Technol. (EML)*, Beijing, China, May 2012, pp. 1–6.

[23] Z. Pantic, S. Bhattacharya, and S. Lukic, "Optimal resonant tank design considerations for primary track compensation in inductive power transfer systems," in *Proc. IEEE Energy Convers. Congr. Expo. (ECCE)*, Atlanta, GA, USA, Sep. 2010, pp. 1602–1609.

[24] Y. Nagatsuka, N. Ehara, Y. Kaneko, S. Abe, and T. Yasuda, "Compact contactless power transfer system for electric vehicles," in *Proc. Int. Power Electron. Conf. (IPEC)*, Sapporo, Japan, Jun. 2010, pp. 807–813.

[25] R. Becker, *Electromagnetic Fields and Interactions*. New York, NY, USA: Dover, 1964.

[26] C. L. Bartberger, "The magnetic field of a plane circular loop," *J. Appl. Phys.*, vol. 21, no. 11, pp. 1108–1114, Nov. 1950.

[27] T. Imura, H. Okabe, and Y. Hori, "Basic experimental study on helical antennas of wireless power transfer for electric vehicles by using magnetic resonant couplings," in *Proc. IEEE Veh. Power Propuls. Conf. (VPPC)*, Dearborn, MI, USA, Sep. 2009, pp. 936–940.

[28] J. Lee and S. Nam, "Fundamental aspects of near-field coupling small antennas for wireless power transfer," *IEEE Trans. Antennas Propag.*, vol. 58, no. 11, pp. 3442–3449, Nov. 2010.

[29] E. L. van Boheeman, J. T. Boys, and G. A. Covic, "Near-field coupled antennas for use in inductive power transfer communication systems," in *Proc. 34th Annu. Conf. IEEE Ind. Electron. (IECON)*, Orlando, FL, USA, Nov. 2008, pp. 1504–1509.

[30] J. B. Sherman, "Some aspects of coupled and resonant circuits," *Proc. IRE*, vol. 30, no. 11, pp. 505–510, Nov. 1942.

[31] J.-R. Sibué, G. Kwimang, J.-P. Ferrieux, G. Meunier, J. Roudet, and R. Périot, "A global study of a contactless energy transfer system: Analytical design, virtual prototyping, and experimental validation," *IEEE Trans. Power Electron.*, vol. 28, no. 10, pp. 4690–4699, Oct. 2013.

[32] F. Nakao, Y. Matsuo, M. Kitsoka, and H. Sakamoto, "Ferrite core couplers for inductive chargers," in *Proc. IEEE Power Convers. Conf. (PCC)*, Osaka, Japan, Apr. 2002, pp. 850–854.

[33] T. Mizuno, S. Enoki, T. Asahina, T. Suzuki, M. Noda, and H. Shinagawa, "Reduction of proximity effect in coil using magnetoplated wire," *IEEE Trans. Magn.*, vol. 43, no. 6, pp. 2654–2656, Jun. 2007.

[34] H. Shinagawa, T. Suzuki, M. Noda, Y. Shimura, S. Enoki, and T. Mizuno, "Theoretical analysis of AC resistance in coil using magnetoplated wire," *IEEE Trans. Magn.*, vol. 45, no. 9, pp. 3251–3259, Sep. 2009.

[35] J. M. Miller, "Wireless charging of plug-in electric vehicles (PEV's)," in *Proc. IEEE Power Electron. Soc. (PELS) Digit. Media Ser.*, Dec. 2011.

[36] J. M. Miller, "New trends in EV's: The need for standards," in *Proc. 1st IEEE Int. Electr. Veh. Conf. (IEVC)*, Greenville, SC, USA, Mar. 2012.

[37] J. M. Miller, "Wireless charging of EV and PHEV batteries," in *Proc. Invited Moderator SAE World Congr.*, Detroit, MI, USA, Apr. 2012.

[38] P. Si, A. P. Hu, S. Malpas, and D. Budgett, "A frequency control method for regulating wireless power to implantable devices," *IEEE Trans. Biomed. Circuits Syst.*, vol. 2, no. 1, pp. 22–29, Mar. 2008.

[39] A. W. Kelly and W. R. Owens, "Connectorless power supply for an aircraft-passenger entertainment system," *IEEE Trans. Power Electron.*, vol. 4, no. 3, pp. 348–354, Jul. 1989.

[40] R. Mecke and C. Rathge, "High frequency resonant inverter for contactless energy transmission over large air gap," in *Proc. IEEE 35th Annu. Power Electron. Specialists Conf. (PESC)*, Aachen, Germany, Jun. 2004, pp. 1737–1743.

[41] J. P. C. Smeets, T. T. Overboom, J. W. Jansen, and E. A. Lomonova, "Comparison of position-independent contactless energy transfer systems," *IEEE Trans. Power Electron.*, vol. 28, no. 4, pp. 2059–2067, Apr. 2013.

[42] S. Jung, H. Lee, C. S. Sung, J.-H. Han, W.-K. Han, and G. Jang, "Optimal operation plan of the online electric vehicle system through establishment of a DC distribution system," *IEEE Trans. Power Electron.*, vol. 28, no. 12, pp. 5878–5889, Dec. 2013.

[43] O. C. Onar, J. M. Miller, S. L. Campbell, C. Coomer, C. P. White, and L. E. Seiber, "A novel wireless power transfer for in-motion EV/PHEV charging," in *Proc. 28th Annu. IEEE Appl. Power Electron. Conf. (APEC)*, Long Beach, CA, USA, Mar. 2013, pp. 3073–3080.

[44] J. M. Miller and O. C. Onar, "Oak Ridge National Laboratory in-motion wireless power transfer system," in *Proc. 1st Conf. Electr. Roads Veh. (CERV)*, Park City, UT, USA, Feb. 2012.

[45] S. Lee, J. Huh, C. Park, N.-S. Choi, G.-H. Cho, and C.-T. Rim, "On-line electric vehicle using inductive power transfer system," in *Proc. IEEE Energy Convers. Congr. Expo. (ECCE)*, Atlanta, GA, USA, Sep. 2010, pp. 1598–1601.

[46] B. Song *et al.*, "Design of a high power transfer pickup for on-line electric vehicle (OLEV)," in *Proc. IEEE Int. Electr. Veh. Conf. (IEVC)*, Greenville, SC, USA, Mar. 2012, pp. 1–4.

[47] J. Shin *et al.*, "Design and implementation of shaped magnetic-resonance-based wireless power transfer system for roadway-powered moving electric vehicles," *IEEE Trans. Ind. Electron.*, vol. 61, no. 3, pp. 1179–1192, Mar. 2014.

[48] J. Huh, S. Lee, C. Park, G.-H. Cho, C.-T. Rim, "High performance inductive power transfer system with narrow rail width for on-line electric vehicles," in *Proc. IEEE 2nd Energy Convers. Congr. Expo. (ECCE)*, Atlanta, GA, USA, Sep. 2010.

[49] J. M. Miller, "Wireless power charging: Stationary & dynamic applications, electric energy systems curriculum for sustainability," in *Proc. ONR/NSF-Sponsored Faculty/Ind. Workshop*, Napa, CA, USA, Feb. 2012.

[50] J. M. Miller, "Beyond hybrid electric vehicles," in *Proc. Invited Presentat. U.S. Dept. Energy Eng., Sci., Technol. Division (ESTD) Dual-Mode Transp. Workshop*, Knoxville, TN, USA, Sep. 2006.

[51] C. H. Stephan, J. M. Millerm, and L. C. Davis, "A programme for individual sustainable mobility," *Int. J. Veh. Auto. Syst.*, vol. 2, nos. 3–4, pp. 255–277, 2004.

[52] M. B. Scudiere, J. W. McKeever, and J. M. Miller, "Design of wireless power transfer for stationary and moving hybrid electric vehicles," in *Proc. SAE World Congr.*, Detroit, MI, USA, Apr. 2011.

[53] J. M. Miller *et al.*, "Demonstrating dynamic wireless charging of an electric vehicle: The benefit of electrochemical capacitor smoothing," *IEEE Power Electron. Mag.*, vol. 1, no. 1, pp. 12–24, Mar. 2014.

[54] N. Mohan, T. M. Undeland, and W. P. Robbins, *Power Electronics: Converters, Applications, and Design*, 2nd ed. New York, NY, USA: Wiley, 1995.

John M. Miller (F'99) received the Ph.D. degree in electrical engineering from Michigan State University, East Lansing, MI, USA, in 1983.

He joined the Scientific Research Laboratory, Ford Motor Company, Dearborn, MI, USA. Following his retirement from Ford Motor Company, he held various engineering and senior management positions in energy storage and electric traction drives. He has been the Program Manager for advanced power electronics and electric machines with the Oak Ridge National Laboratory, Oak Ridge, TN, USA, until 2014. He is currently a Principal Engineer with his consulting business, and a Leader in high-power wireless charging.

Dr. Miller is a fellow of the Society of Automotive Engineers, and a Registered Professional Engineer in Michigan and Texas. He is a member of the Scientific Advisory Board to Momentum Dynamics.

Omer C. Onar received the Ph.D. degree in electrical engineering from the Illinois Institute of Technology, Chicago, IL, USA, in 2010.

He joined the Power Electronics and Electric Machinery Group, Oak Ridge National Laboratory (ORNL), Oak Ridge, TN, USA. His current research interests include transportation electrification, wireless power transfer systems, and renewable energies.

Dr. Onar was a recipient of the Alvin M. Weinberg Fellowship at ORNL.

Madhu Chinthavali received the B.E. degree in electrical engineering from Bharathidasan University, Tiruchirappalli, India, in 2000, and the M.S. degree in electrical engineering from the University of Tennessee, Knoxville, TN, USA, in 2003.

He is currently a Staff Member and Team Leader with the Power Electronics and Electric Machinery Group, Oak Ridge National Laboratory, Oak Ridge, TN, USA.